Physical and mechanical properties of winter first-year ice in the Antarctic marginal ice zone along the Good Hope Line

Sebastian Skatulla[1,4], Riesna R. Audh[2,4], Andrea Cook[1,4], Ehlke Hepworth[2,4], Siobhan Johnson[3,4], Doru C. Lupascu[5], Keith MacHutchon[1,4], Rutger Marquart[1,4], Tommy Mielke[5], Emmanuel Omatuku[1,4], Felix Paul[5], Tokoloho Rampai[3,4], Jörg Schröder[6], Carina Schwarz[6], and Marcello Vichi[2,4]

[1]University of Cape Town, Department of Civil Engineering, South Africa
[2]University of Cape Town, Department of Oceanography, South Africa
[3]University of Cape Town, Department of Chemical Engineering, South Africa
[4]Marine and Antarctic Research Centre for Innovation and Sustainability (MARIS), University of Cape Town, South Africa
[5]University of Duisburg-Essen, Institute for Materials Science and Center for Nanointegration Duisburg-Essen (CENIDE), Germany
[6]University of Duisburg-Essen, Institute of Mechanics, Germany

Correspondence: Sebastian Skatulla (sebastian.skatulla@uct.ac.za)

Abstract. As part of the 2019 Southern oCean seAsonal Experiment (SCALE) Winter Cruise of the South African icebreaker SA Agulhas II first-year ice was sampled at the advancing outer edge of the Antarctic marginal ice zone along a $150\,\mathrm{km}$-Good Hope Line transect. Ice cores were extracted from four solitary pancake ice floes of $1.83 - 2.95\,\mathrm{m}$ diameter and $0.37 - 0.45\,\mathrm{m}$ thickness as well as a $12 \times 4\,\mathrm{m^2}$ pancake ice floe of $0.31 - 0.76\,\mathrm{m}$ thickness part of a larger consolidated pack ice domain. The ice cores were subsequently analysed for temperature, salinity, texture, anisotropic elastic properties and compressive strength. All ice cores from both, solitary pancake ice floes and consolidated pack ice, exhibited predominantly granular textures. The vertical distributions of salinity, brine volume and mechanical properties were significantly different for the two ice types. High salinity values of $12.6 \pm 4.9\,\mathrm{PSU}$ were found at the topmost layer of the solitary pancake ice floes but not for the consolidated pack ice. The uniaxial compressive strength for pancake ice and consolidated pack ice were determined as $2.3 \pm 0.5\,\mathrm{MPa}$ and $4.1 \pm 0.9\,\mathrm{MPa}$, respectively. The Young's and shear moduli in longitudinal core direction of solitary pancake ice were obtained as $3.7 \pm 2.0\,\mathrm{GPa}$ and $1.3 \pm 0.7\,\mathrm{GPa}$, and for consolidated pack ice as $6.4 \pm 1.6\,\mathrm{GPa}$ and $2.3 \pm 0.6\,\mathrm{GPa}$, respectively. Comparing Young's and shear moduli measured in longitudinal and transverse core directions, a clear directional dependency was found, in particular for the consolidated pack ice.

1 Introduction

The seasonal sea ice advance and retreat in the Antarctic Marginal Ice Zone (MIZ) of the Southern Ocean (SO) is heavily influenced by harsh atmospheric and oceanic conditions. Accordingly, its sea ice properties are characterised by high temporal and spatial fluctuations and still elude reliable prediction by current climate models (Hobbs et al., 2016). Due to the limited in situ data from the Antarctic region throughout the year, well established sea ice rheology models such as (Hibler III, 1979; Wang and Shen, 2010) are phenomenological approaches considering only effective properties of spatially variable ice concentration

20 and empirically-derived thickness and mechanical properties. In this sense, these models are not informed by the underlying mechanisms and phenomena defining sea ice behaviour, and the model parameters have little physical meaning. Therefore, a generalization of these models to sea ice conditions other than those for which they were fitted to is problematic (Squire, 2018).

Clearly, more investigation of early-stage ice formation in the Antarctic MIZ is necessary to elucidate the seasonal evolution of the ice morphology and to link the physical and mechanical properties from the sub-millimeter to kilometer-scale, as this

25 stage defines the ice properties also later at the consolidated and melting stages. In order to acquire an in-depth understanding of sea ice characteristics and improve forecasting of sea ice trends, short term and long term, remote observational sea ice data and their reanalysis products need to be cross-referenced with in situ observations comprising the actual degree of ice consolidation, thickness, floe size, material composition and morphology. In particular, the mechanics of sea ice in terms of deformation, fracture and faulting is linked to a range of spatial and temporal scales (Weiss and Dansereau, 2017).

30 On a smaller scale less than $10\,\mathrm{km}$, ice strength is distinctly heterogeneous and anisotropic due to the occurrence of leads (Hutchings and Hibler III, 2008). Also, the distribution of floe characteristics such as size, shape, thickness and concentration becomes significant, in particular in the marginal ice zone (Hutchings et al., 2012; Bennetts et al., 2017; Roach et al., 2018; Marquart et al., 2021). Owing to the rough sea states in winter SO delaying sea ice consolidation and rafting effects, sea ice morphology is vertically changing in terms of grain size, crystallographic texture and fabrics as well as porosity (Timco and

35 Weeks, 2010; Dempsey and Langhorne, 2012). On the meter-scale and smaller, the mechanical behaviour of sea ice comprises elastic, inelastic, brittle and viscous material characteristics which are directly related to its grain and pore structure, brine inclusions as well as the generally temperature and strain rate-dependent material response (Mellor, 1986; Schulson et al., 2006). Short-term and seasonal atmospheric temperature fluctuations, precipitation and associated brine drainage processes are continuously altering sea ice composition and properties (Wells et al., 2011; Galley et al., 2015; Thomas et al., 2020).

40 Accordingly, the mechanical ice properties need to be put into context with ice salinity, temperature, density, porosity, type as well as crystal size and orientation (Nakawo and Sinha, 1981; Kovacs, 1996; Timco and Weeks, 2010).

This paper will report on the sampling and testing of winter first-year ice at the edge of the Antarctic marginal ice zone along the Good Hope Line during the 2019 SCALE[1] Winter Cruise. It is the first winter expedition dedicated to MIZ measurements in the eastern Weddell Sea region after the earlier observations in the late 1980s and early 1990s (e.g. Lange et al. (1989),

45 Eicken et al. (1994), Kivimaa and Kosloff (1994b) and Haas et al. (1992)). The focus is on the physical and mechanical properties of sea ice in the MIZ from the edge into more consolidated pack ice conditions. The properties determined include sea ice morphology, temperature, bulk salinity, bulk density, elastic properties, uniaxial compressive strength as well as snow thickness and salinity.

The plan of this paper is as follows: Sec. 2 elaborates on sampling and testing methods, Sec. 3 describes and discusses

50 physical and mechanical data obtained, and a summary of the findings is provided in Sec. 4.

---

[1]Southern oCean seAsonal Experiment http://scale.org.za/

2 Materials and Methods

2.1 Sample collection

The 2019 Winter SCALE cruise started with the SA Agulhas II departing from Cape Town on the July 18, 2019 sailing directly south to the Antarctic MIZ. The ship entered the ice on the July 26, 2019 at 1pm and exited on the July 28, 2019 at 8:30pm.
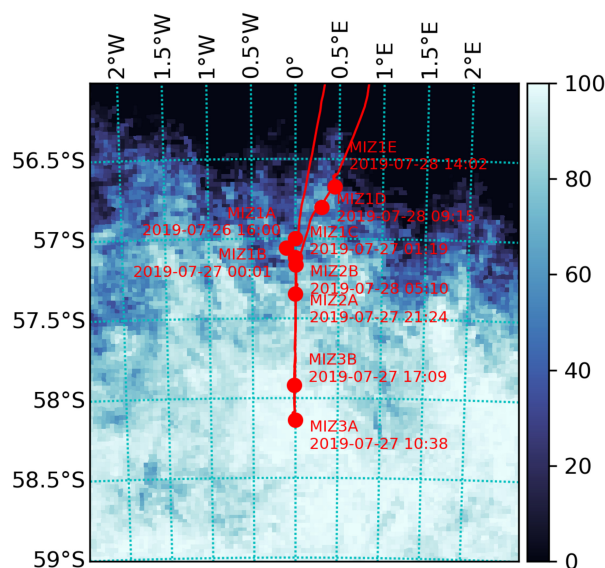
Figure 1. Map of the ice stations with date and time of the starting of operations. The ship entered from the westernmost course and exited from the easternmost course. The sea ice concentration chart was obtained from the University of Hamburg ASI-AMSR2 processing for the July 26, 2019, concentration values in %.

An overview of the MIZ stations is shown in Fig. 1 with the naming convention and corresponding coordinates listed in Tab. 1. The station plan was designed to resolve the evolution of sea ice features from the open ocean into more consolidated sea ice conditions. Due to contingency and time optimization, the sequence of stations did not follow the original design. The naming convention was extended to preserve the original geographic distribution of MIZ1X being at the edge with the open ocean and MIZ3X in consolidated pack ice. Stations were therefore turned into clusters, where overboard ice coring, pancake ice collection, grease ice sampling, buoy deployment, environmental measurements and ocean sampling took place. Additional biogeochemical sampling was performed at MIZ2X which is, however, not part of this work.

A complete set of sea ice observations was done every hour from the bridge commencing on July 26, 2019 at 1pm and ended on July 28, 2019 at 8:30pm when entering and exiting the ice, respectively. Observations were collected according to the Antarctic Sea Ice Processes and Climate (ASPeCt) protocol estimating ice concentration, ice type, floe size and thickness, cloud cover, visibility, weather, and air and sea surface temperature. The initially higher frequency observations where eventually combined into the hourly frequency required by ASPeCt (Hepworth et al., 2020).

Table 1. List of ice sampling stations.

Station	Start Date & Time	Latitude	Longitude
MIZ3A	July 27, 2019 10:38am (UTC)	S 58.13783	W 0.00442
MIZ1D	July 28, 2019 9:15am (UTC)	S 56.80178	E 0.30262
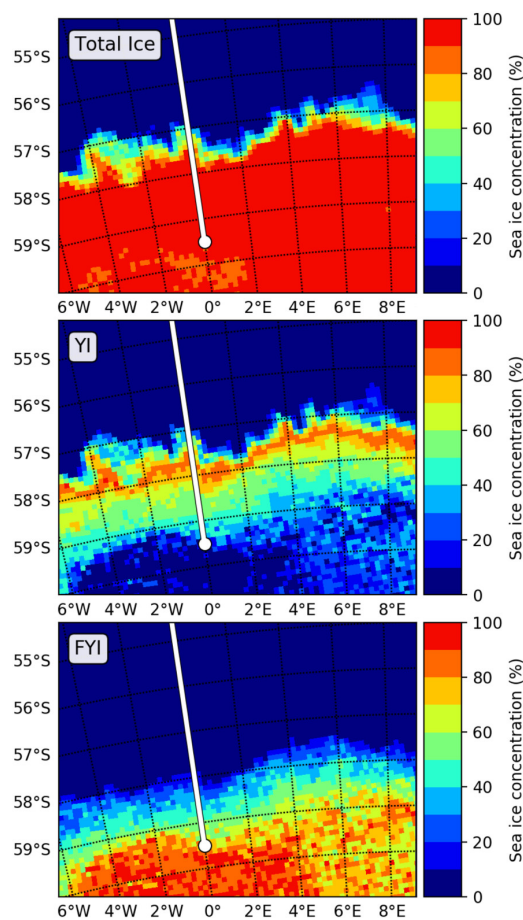
Figure 2. Sea ice type concentration data provided by the University of Bremen. Daily concentration of total ice, young ice (YI) and first-year ice (FYI) on the July 24, 2019 prior to the ship entering the MIZ. The cruise plan and the southernmost station (MIZ3A) are also shown. Data are available at https://seaice.uni-bremen.de/data/MultiYearIce

The first ice floes were observed in the early afternoon of the July 26, 2019. Sea ice features were rapidly varying and large expanses of consolidated pack ice were found at the latitude of MIZ3. Ice navigation and planning was assisted by i) ice edge charting based on satellite data and reanalysis products by the South African Weather Service (SAWS) (de Vos et al., 2021),

70   and ii) a prototype remote sensing product describing multi-year ice concentration and other sea ice types developed by the
University of Bremen (Melsheimer and Spreen, 2021). The latter distinguishes the different ice types (young ice, first-year ice
and multi-year ice) based on the combination of passive microwave and scatterometer data using an algorithm developed by
Environment Canada's Ice Concentration Extractor (ECICE) (Shokr and Agnew, 2013) and corrections by Ye et al. (2015).
Fig. 2 shows that the southernmost ice station was expected to be predominantly in first-year ice (FYI) conditions, which was

75   confirmed on site. The MIZ with unconsolidated ice conditions, composed of pancake ice floes of about 1 to 5 m-diameter,
likely extended for about 200 km southward as indicated by the young ice (YI) map features in Fig. 2.

Fieldwork operations involving ice core sampling took place on the southward-bound leg at the most southerly station,
MIZ3A, as shown in Fig. 1 on July 27, 2019 between 10am-4pm (UTC). Operations took place at daylight in harsh conditions.
The air temperature was $-17\,°C$ and the wind speed $20\,m\,s^{-1}$, according to the on-board equipment of the South African

80   Weather Services. Large first-year floes, ranging between 500-2000 m in diameter, completely covered the ocean, each one
composed of cemented pancake ice floes of smaller sizes. The coring and temperature measurement of cores were done on a
single pancake ice floe, about $12\,m \times 4\,m$ in dimensions, part of a larger consolidated pack ice domain located off the starboard
bow as shown in Fig. 3. All cores were extracted in vertical direction, perpendicular to the ice floe surface. The equipment

Figure 3. Coring field at MIZ3A showing the cemented pancakes with sizes varying between 3 and 15 m.

used on the ice during the sampling activity consisted of a corer, temperature probes, a plastic rail to fixate the core during

85   the temperature measurements, a crate with a 5 cm-styrofoam insulation, a 3D printed Niskin bottle and other equipment
used to collect and store snow cover samples. The coring equipment comprised a 1 m-long 9 cm-diameter Kovacs Mark II
barrel operated with an electric drill. For temperature measurements, a cordless drill, the Testo GMH 3750-GE logger ($\pm 0.03°$
system accuracy) with high precision Pt100 penetration probes GTF 401 1/10 DIN ($\pm 0.03°$ accuracy) were utilized (Testo,
Titisee-Neustadt, Germany).

90   A total of 26 cores were collected, each for a dedicated type of testing, with the core IDs and corresponding names found in App. A1 in Tab. A1. The length of the cores is representative of the pack ice thickness. Three of them were immediately processed after coring to determine the vertical temperature distribution. For this purpose, the cores were placed on a plastic rail with markings for drill points $5\,\mathrm{cm}$ apart from each other. The temperature probe was put into pre-drilled holes, and temperature readings were recorded. All readings were completed within 4 minutes of coring. After sea ice core collection, a

95   3D printed Niskin bottle was deployed through two core cavities to retrieve samples of the water at the ice-ocean interface. The Niskin 3D deployment yielded two water samples of approximately $700\,\mathrm{ml}$ each from which the boundary layer salinity of the ocean was determined by a Portasal salinometer. The remaining cores were subsequently taken aboard for further processing in the glaciological Cold Laboratory or stored in the ship's freezer. The temperature in the laboratory was kept at $-10\,^\circ\mathrm{C}$ and the ship's freezer was maintained at $-25\,^\circ\mathrm{C}$, respectively. The cores were continuously kept in a horizontal position during

100   transport and storage to minimize further brine drainage.

    The collection of solitary pancake ice floes took place on the northward-bound leg at the second most northerly station, MIZ1D, on July 28, 2019 between 10:45am-4pm (UTC). Station MIZ1D was characterized by 80% of the ocean surface covered by pancake ice floes of about 1-$3\,\mathrm{m}$ diameter as shown in Fig. 4. The relatively warmer air temperature and lower wind speed were recorded at $-8\,^\circ\mathrm{C}$ and $12\,\mathrm{m\,s^{-1}}$, respectively, and a dampened swell was observed. The calm ocean and wind

105   conditions allowed for the quick selection and isolation of pancake ice floes. The pancakes were collected from the ocean using the helideck crane and a custom-made $5 \times 5\,\mathrm{m^2}$ heavy-duty net held by a spreader beam construction designed for a maximum payload of $3.5\,\mathrm{t}$.

Figure 4. Sampling of solitary pancake ice floes with diameters of about $2.5\,\mathrm{m}$ using the ship's crane.

    Four pancake ice floes, labelled A to D, were collected and placed onto individual wooden grids as depicted in Fig. 5 to ease coring and prevent the contamination by the ship deck. Details on the different pancake dimensions are given in Tab. 2.

Figure 5. Pancake ice floes placed on wooden grids on the ship's helideck: Pancake A (top left), Pancake B (top right), Pancake C (bottom left) and Pancake D (bottom right) shattered into six large pieces during removal from the net.

Table 2. Overview of pancake ice floe dimensions.

Pancake ice floe		A	B	C	D
	Height	0.40	0.37	0.45	0.37
Dimensions [m]	Length	2.42	2.49	2.40	2.95
	Width	1.83	2.33	2.33	2.51

110   All four pancakes had rafted edges, were snow-covered and did not have a visibly discoloured biologically active layer. The depth and temperature of the snow-layer was taken before each pancake was manoeuvred out of the net which is found in Tab. 2. During the pancake ice floe lifting, the 3D printed Niskin bottle was again deployed from the helideck to retrieve water samples from which the ice-ocean boundary layer salinity was determined. In addition, interstitial frazil ice was collected and its viscosity was measured, further details are found in Paul et al. (2021).

115   Subsequently, between 17 and 23 cores were obtained from each pancake ice floe. The corresponding coring layout with core IDs and corresponding names can be found in App. A1 in Fig. A1 and Tab. A2-A5, respectively. As for the pack ice, all cores were extracted in vertical direction, perpendicular to the ice floe surface. As such, the length of the cores is representative of the pancake ice floe thickness (depth). For each floe, three cores were tested to determine the vertical temperature profile

immediately after the floe had been off-loaded. All cores were subsequently transferred to either the Cold Laboratory for further

120 processing and testing, or to the ship's freezer.

2.2 Testing of physical and mechanical properties

The ice cores used to profile the vertical temperature distribution in consolidated pack ice and pancake ice were subsequently cut with a stainless steel band saw into segments close to $10\,\mathrm{cm}$-length and allowed to melt in ziploc bags in a refrigerator at $5\,°\mathrm{C}$. Once melted, the volume of the samples was measured using a graduated beaker and the bulk salinity was obtained by

125 means of a Portasal salinometer.

Based on the obtained temperature and salinity data, the brine volume distributions in pancake ice and consolidated pack ice were determined via the empirical relations by Frankenstein and Garner (1967)

$$V_b = S_i \left(\frac{49.185}{T} + 0.532 \right) \tag{1}$$

where V_b denotes brine volume [%], S_{si} [PSU] the bulk salinity and T [°C] the temperature.

130 The morphology of sampled pancake and consolidated pack ice was studied with respect to crystal structure, stratigraphy and texture. For this purpose, one ice core at consolidated conditions and further four pancake ice cores were investigated. The ice cores were visually inspected already during extraction to record obvious physical features such as thickness of snow topping, layering in the texture of the ice, and the presence of possible defects such as cracks. The cores were then taken directly to the ship's storage facility and analysed back at the University of Cape Town, approximately 6 months after collection being stored

135 at $-20\,°\mathrm{C}$. The cores were first cut into $10\,\mathrm{cm}$-segments and longitudinal sections with thicknesses in the order of $8\,\mathrm{mm}$ were then cut from the centre of these segments with a stainless steel band saw at $-10\,°\mathrm{C}$ laboratory temperature. These $8\,\mathrm{mm}$-thick sections were further cut using a thermal macrotome to create thin sections of $1\,\mathrm{mm}$ thickness and subsequently viewed through cross-polarised sheets and photographed. The cross-polarised photographs were subsequently analysed for their respective ice textures and crystal sizes. From these images, stratigraphy diagrams were composed for easy visual comparison between cores

140 and the average crystal sizes measured.

The testing of anisotropic elastic material properties of sea ice was conducted in the ship's Cold Laboratory at $-10\,°\mathrm{C}$ within a few hours after collection. Since the mechanical behaviour of sea ice is rate-dependent, the Young's modulus is typically determined measuring the speed of ultrasonic waves, a pressure and shear wave, travelling through the ice to exclude viscous strain in the deformation response (Timco and Weeks, 2010). The P- and S-wave signals are initiated by a pair of

145 transducers put on opposite surfaces of a specimen. The Young's and shear moduli can then be calculated on the basis of its length (the distance between the transducers), its bulk density as well as the speed of transmission of the P- and S-waves in accordance with the following formulae (Snyder et al., 2015):

$$E_i = \rho c_s^2 \frac{3c_p^2 - 4c_s^2}{c_p^2 - c_s^2}, \tag{2}$$

$$G_i = \rho c_s^2, \tag{3}$$

where E_i and G_i denote the Young's and shear moduli, respectively, associated with the material direction x_i, ρ the bulk density of ice, c_p the transmission speed of the P-wave and c_s the transmission speed of the S-wave, both measured along direction x_i.

The 9 cm-diameter cores ranging between 30-45 cm in length were first visually inspected in the laboratory to identify any internal cracking or other defects that could affect the ultrasound testing results. Subsequently, it was planned how to segment the cores into specimen lengths as close to 10 cm as possible for testing, see Fig. B1 in App. B. At this stage, consideration was given to already existing segmentation due to fracturing occurred at time of core extraction. The cores were then cut into the planned segments along the entire length using a stainless steel bandsaw providing clean parallel surfaces at the end faces on either side for the subsequent ultrasound measurements in the longitudinal ice core direction. For measurements in the transverse core direction, each segment was again cut in longitudinal direction at two parallel opposite sides providing the required flat surfaces to apply the transducers. These two surfaces were $7.2\,\mathrm{cm} \pm 0.8\,\mathrm{cm}$ and $7.1\,\mathrm{cm} \pm 1.3\,\mathrm{cm}$ apart from each other for pancake and consolidated pack ice specimens, respectively. In order to determine the bulk density of the 43 specimens, their dimensions and weight was first measured, the latter using a hand-held scale. The ultrasound testing was carried out less than two hours after core extraction using a PROCEQ Pundit PL-200 testing kit (Screening Eagle Technologies, Schwerzenbach, Switzerland with 250 kHz P- and S-wave transducers assuming that the mechanical properties of the ice cores had not significantly changed by that time (Pustogvar and Kulyakhtin, 2016). A low-temperature silicon grease applied to the transducer faces ensured the best possible contact with the ice specimens for the transfer of P- and S-waves across the interface. Three separate tests were carried out for each specimen and direction.

The compressive strengths of the ice samples were determined using the GCTS PLT-2W wireless unconfined compression testing device (GCTS Testing Systems, Tempe, USA). Samples with a height up to 13.5 cm can be accommodated. There are no constraints induced by the platens to avoid a triaxial state of stress. The cores were cut via a stainless steel bandsaw into multiple 13.5 cm-long segments and immediately tested. In the interest of time to minimize brine drainage and alterations to the ice morphology, it was deliberately decided not to reduce the sample's diameter required for the optimal diameter/length-ratio of 1:2.5 (Schulson and Duval, 2009). In total, 27 compression testing specimens were obtained from twelve pancake ice and three pack ice cores. Specimen dimensions and names are displayed in App. B in Fig. B2. The specimen naming convention is derived from the core names with an additional numbered postfix (S1-S6) indicating the consecutive specimen segmentation sequence starting from the top of the core. The compression testing commenced less than two hours after core extraction. The uniaxial compression load was manually applied to the sample by a hand pump with an approximate strain rate of $2 \times 10^{-4}\,\mathrm{s}^{-1}$ to $6 \times 10^{-4}\,\mathrm{s}^{-1}$.

3 Results and discussion

3.1 Temperature, salinity, porosity and density

The vertical temperature profiles for consolidated pack ice and pancake ice floes A, B and D illustrated in Fig. 6 exhibit the typical linear distribution with depth (Nakawo and Sinha, 1981; Petrich and Eicken, 2017). The temperature gradient of
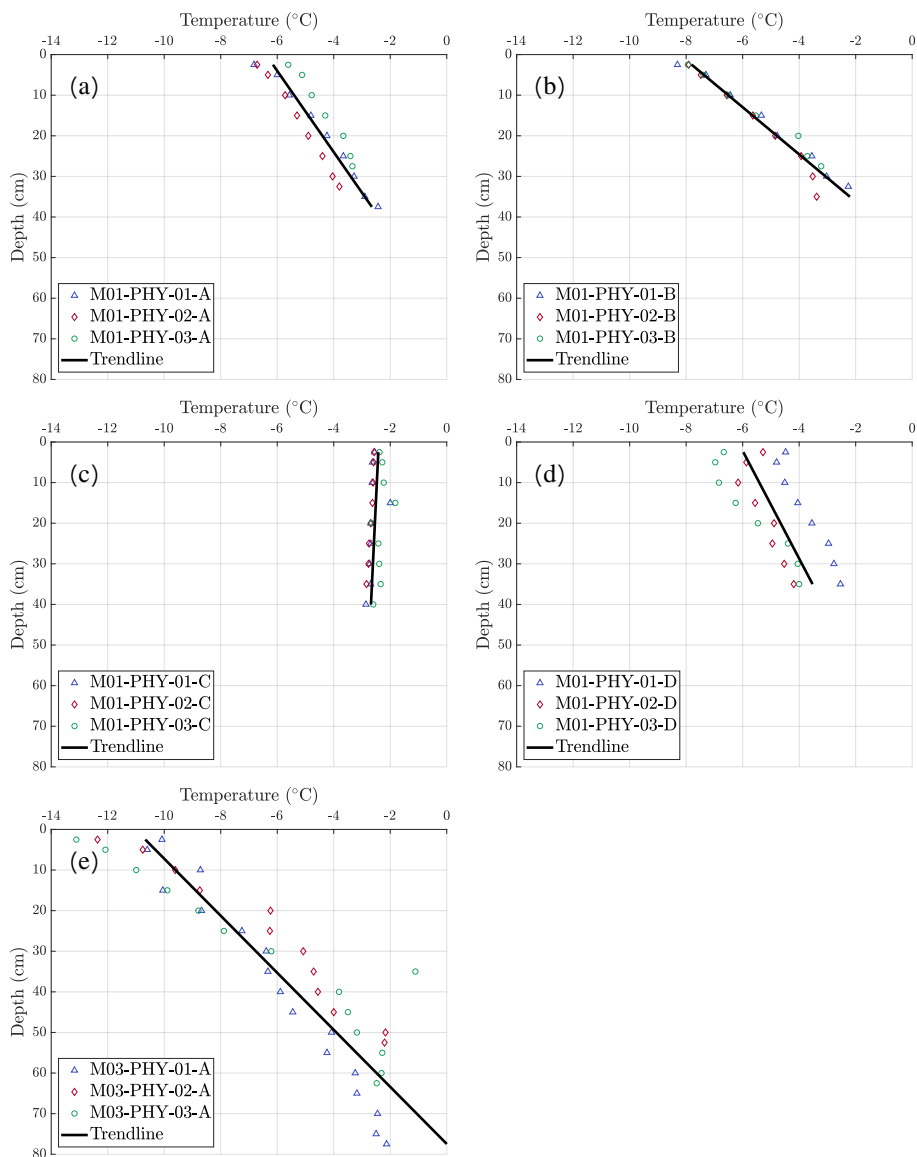
Figure 6. Plots of temperature over sea ice depth for the four pancake ice floes (cores M01-PHY-01-A/B/C/D, M01-PHY-02-A/B/C/D, M01-PHY-03-A/B/C/D) and for the consolidated pack ice (cores M03-PHY-01-A, M03-PHY-02-A and M03-PHY-03-A), respectively.

the former is considerably larger due to the lower atmospheric temperature on the day of sampling and testing. However, for pancake ice floes C, the temperature distribution is nearly constant and rather high temperature values were recorded, in particular toward the top core sections. Accordingly, its consistency was reported to be rather soft and poorly consolidated except for the very top. A significant influence of the snow cover on this disparity can be ruled out, as only minor snow cover was found as listed in Tab. 3 and shows only small variations between all four pancakes. The substantially increased

temperatures and porous texture of pancake ice floe C are exhibited in particular in top and middle core sections, a potential explanation could therefore be overwashing occurred during collection and subsequent vertical drainage. This is also further

190 substantiated by the temperature measurements of the thin snow layers covering the four pancake ice floes performed on deck providing $-2.8 \pm 0.1\,°C$ which indicates overwashing as it should be closer to the measured atmospheric temperature of $-8\,°C$. Furthermore, the snow temperatures do not link to their respective pancake ice floe temperature profiles, except of pancake ice floe C. It has been reported from ice floe-mounted SIMBA measurements of storm-caused ice floe flooding events that subsequent significant heat propagation occurred increasing ice temperature from initially $-8.5\,°C$ at the top surface by about

195 $3\,°C$ down to $70\,cm$ depth (Provost et al., 2017).

The boundary layer salinity of the ocean was determined as 33.29 and 34.11 PSU at MIZ3A and MIZ1D, respectively. The vertical salinity profile for the pancake ice floes depicted in Fig. 7 exhibits at the top of pancake ice floes with $12.6 \pm 4.9\,PSU$ significantly higher values than below with $5.8 \pm 1.1\,PSU$. The high salinity of the topmost core section is generally attributed to the high initial growth rate and lower permeability of fine-grained granular ice (Nakawo and Sinha, 1981). This can be

200 confirmed by the stratigraphy of the cores of pancake ice floes A, B and C which are entirely composed of granular ice as shown in Fig. 10. The obtained values compare to in situ data of congealed grease ice in an artificial lead by Smedsrud and Skogseth (2006). On the other hand, in situ experiments in the Arctic by Notz and Worster (2008) demonstrated that initially high salinity values at the topmost parts giving the characteristic C-shape vanish due to gravity drainage within $48\,hrs$, if the frazil ice layer is thin. This would explain the generally low salinity values at the top of the sampled consolidated pack ice of

205 4.4-7.4 PSU where the topmost granular layer is only about $5\,cm$-thick as shown in Fig. 10 and is immediately followed by a columnar layer.

Table 3. Overview of pancake ice floe snow depth and salinity.

Pancake ice floe	A	B	C	D
Snow depth [cm]	2.5	3.5	3.6	3.5
Snow salinity [PSU]	24.74	18.43	9.68	14.26

The snow depth and salinity measurements of the pancake ice floes is listed in Tab. 3. The snow salinity is noticeably higher than the salinity found at the topmost core sections of pancake ice floe A, B and D pointing at surface flooding which was also found for East-Antarctic sea ice (Massom et al., 1998). For floe C the salinity measurements in snow and underlying ice are of

210 a similar magnitude. The latter might be connected to significant overwashing and drainage occurred during floe collection as mentioned before.

Due to brine drainage, the computed brine volume in consolidated pack ice is generally lower than in pancake ice (Notz and Worster, 2008) which is confirmed by the computed brine volume data illustrated in Fig. 8. As the measured salinity in consolidated pack ice is fairly constant with $6.0 \pm 1.5\,PSU$, the brine volume increases with temperature and depth ($r = 0.866$,

215 $n = 20$, $p < 0.001$). The opposite is found for pancake ice where the brine volume clearly decreases with depth ($r = -0.382$, $n = 40$, $p = 0.015$), as the salinity values at the topmost sections are significantly higher compared to the lower sections.
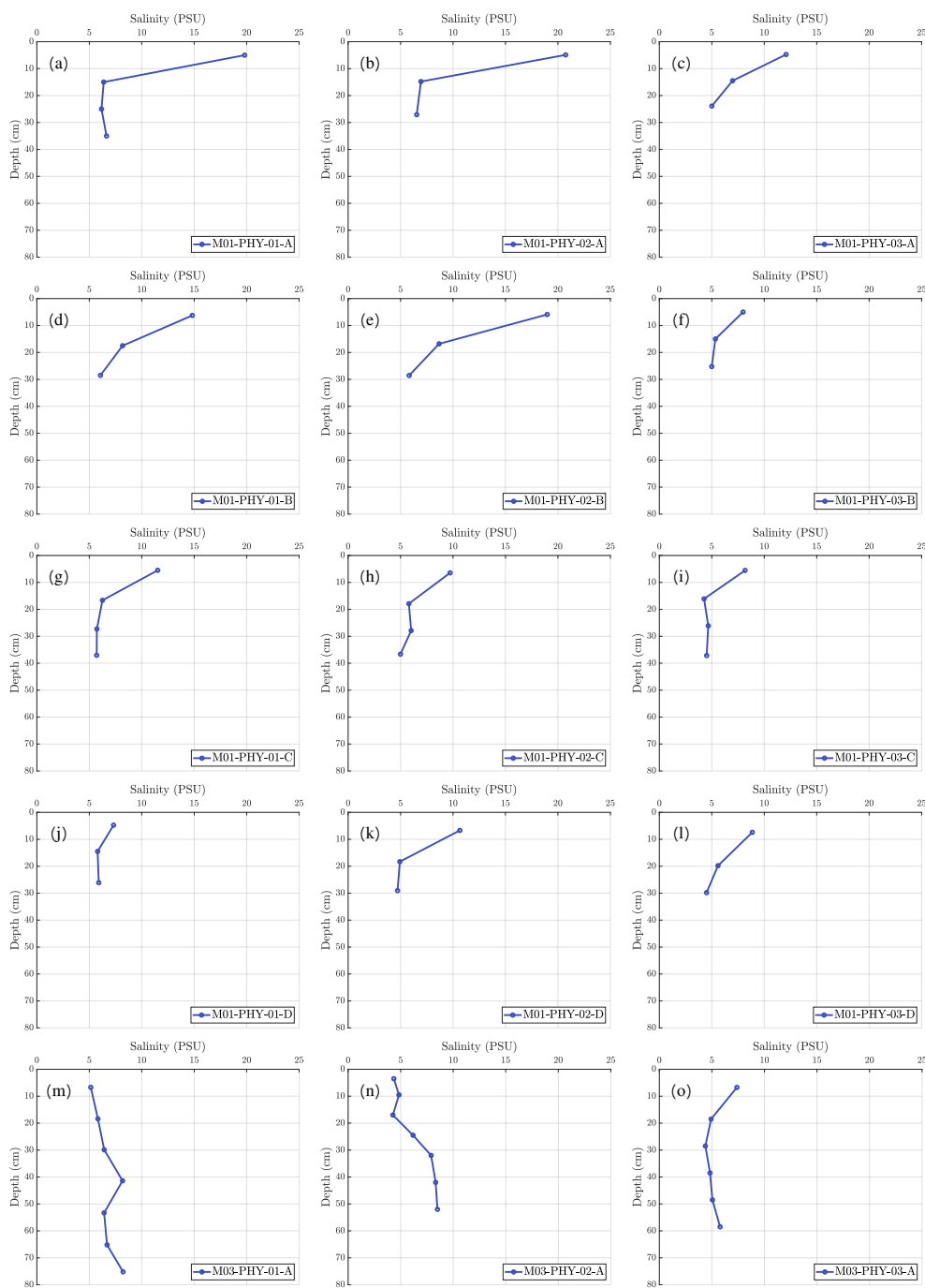
Figure 7. Plots of salinity over sea ice depth for the four pancake ice floes (cores M01-PHY-01-A/B/C/D, M01-PHY-02-A/B/C/D, M01-PHY-03-A/B/C/D) and for the consolidated pack ice (cores M03-PHY-01-A, M03-PHY-02-A and M03-PHY-03-A), respectively.
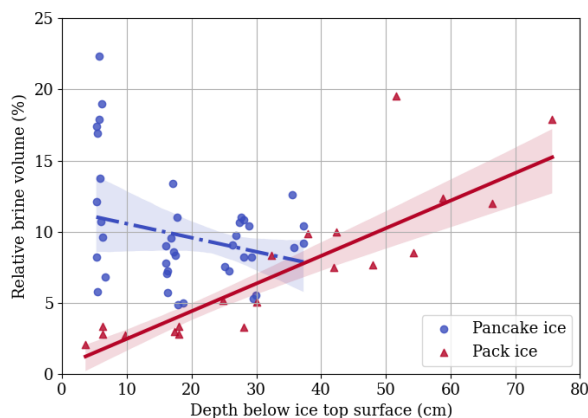
Figure 8. Brine volume as a percentage of the total volume as a function of depth for pancake ice floes and consolidated pack ice at stations, MIZ1D and MIZ3A, respectively. The shading indicates the 90-percentile confidence intervals.
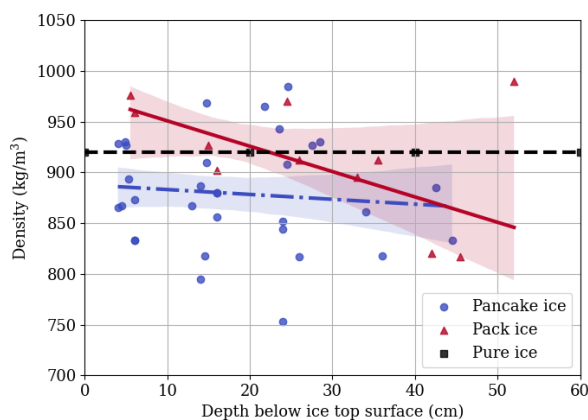
Figure 9. Bulk density as a function of depth for pancake ice floes and consolidated pack ice at stations, MIZ1D (cores M01-US-01A/B/C/D, M01-US-02A/B/C/D) and MIZ3A (cores M03-US-01-A and M03-US-02-A), respectively. The shading indicates the 90-percentile confidence intervals.

Considering that the density values for pancake ice illustrated in Fig. 9 are with $879 \pm 53.5\,\mathrm{kg\,m^{-3}}$ noticeably lower than that of pure ice, a significant air volume fraction is indicated. The measured bulk density results for the top parts of consolidated pack ice illustrated are not plausible, as it would correspond to very high salinity values which have not been observed. There is no significant correlation between density and depth for pancake ice ($r = -0.103$, $n = 32$, $p = 0.576$) and pack ice ($r = -0.426$, $n = 11$, $p = 0.192$).

3.2 Morphology

Three different ice textures can be identified in the cores, namely granular, transitional and columnar. Granular textures, associated with the initially formed frazil ice and also meteoric ice (Massom et al., 1998), have the smallest crystal grain sizes
225 with the former exhibiting rounded and convex shapes, and the latter isometric grains with planar boundaries (Eicken, 1998). Orbital granular ice is formed by the coagulation and freezing together of frazil ice crystals whereas polygonal granular ice of meteoric origin is due to snow mixing with ocean water in the frequently observed flood pools on pancake ice floes due to overwashing which is a common phenomenon in the Ross, Amundsen, Bellingshausen and Weddell seas (Jeffries et al., 1994; Eicken et al., 1995; Sturm et al., 1998). The proportion of snow ice is significant in particular in Antarctic sea ice due to
230 abundance of precipitation and severe sea states (Lange et al., 1990; Worby et al., 1998; Jeffries et al., 2001; Bromwich et al., 2004). Columnar ice textures display large, elongated crystals while transitional textures display a mixture of granular and columnar textures, thus its defining features are small crystals that are beginning to elongate and lengthen into the distinctly columnar ice.

A summary of the fraction of ice textures found to be present in each core along with their respective crystal sizes is found
235 in Tab. 4, while the stratigraphy diagrams are illustrated in Fig. 10. The stratigraphy diagrams are a summary showing the vertical layering of the ice textures within the sampled sea ice. The pancake ice floes A, B and C are completely comprised of

Table 4. Summary of the sea ice core textures. μ specifies the 95-percentile confidence intervals.

| Station-Floe | Granular | | Transitional | | Columnar | |
	Fraction	Crystal Size [mm]	Fraction	Crystal Size [mm]	Fraction	Crystal Size [mm]
MIZ1D-A	1	2.06	-	-	-	-
MIZ1D-B	1	2.31	-	-	-	-
MIZ1D-C	1	1.77	-	-	-	-
MIZ1D-D	0.5	1.38	0.5	4.34	-	-
MIZ3A	0.84	2.58	0.067	7.55	0.093	15.6
	$1.87 < \mu < 2.17$		$4.77 < \mu < 6.23$		-	

granular ice as shown in Fig. 10 which is expected of young pancake ice found at the edge of the Antarctic marginal ice zone where frazil ice generation is prevalent due to the harsh sea states in winter (Lange and Eicken, 1991). It is known from in situ observations in the Arctic that the grease ice layer thickness can reach more than $40 \, \mathrm{cm}$ before congealing under turbulent and
240 dynamic conditions characterized by convective overturning and wind-driven frazil accumulation (Smedsrud and Skogseth, 2006). Pancake ice floe D also displays transitional ice textures indicating the beginning of downward freezing due to calmer sea state and wind conditions (Weeks and Ackley, 1982). The variability in the pancake ice floes is hard to quantify with
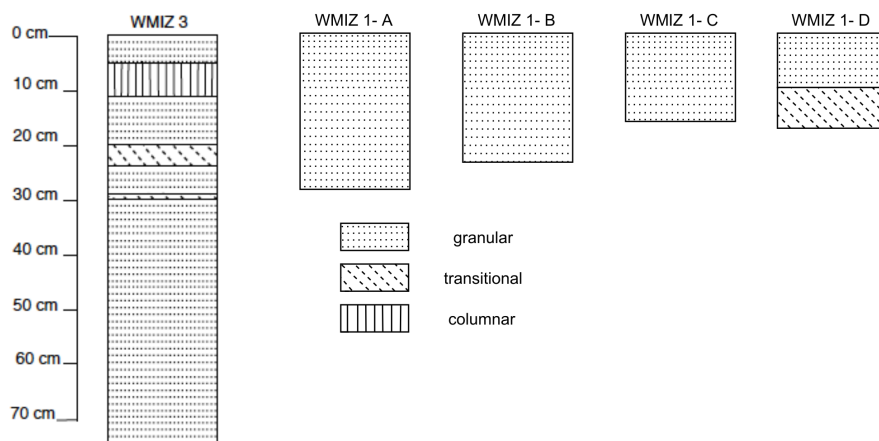
Figure 10. Stratigraphy diagrams for consolidated pack ice core M03-CP-01-A (WMIZ 3) and pancake ice cores M01-CP-01-A (WMIZ 1-A), M01-CP-01-B (WMIZ 1-B), M01-CP-01-C (WMIZ 1-C) and M01-CP-01-D (WMIZ 1-D), respectively.

regards to their morphology due to their young age. The size range of the granular crystals varies, with pancake ice floe A and C being statistically dissimilar.

245   The consolidated pack ice core clearly indicates the presence of different layers and is found to be made up of 84 % granular crystals. As previously mentioned, this is generally indicative of fairly turbulent ice growth conditions leading to significant frazil ice generation. Small bands of columnar and transitional ice textures were found sandwiched between granular ice which is typical of young ice grown in a highly dynamic ocean environment where regularly occurring atmospheric storms can interrupt steady growth of the ice, causing the morphology of the ice crystals and grain structures to vary in type, size and 250   orientation during the growth period of the ice (Lange and Eicken, 1991; Carnat et al., 2013; Shokr and Sinha, 2015).

3.3   Elastic properties and density

The dynamic Young's and shear moduli measurements for consolidated pack ice and pancake ice are shown in Figs. 11 and 12, respectively. For the pancake ice, there is no significant correlation between Young's modulus and depth in longitudinal direction ($r = 0.120$, $n = 32$, $p = 0.513$) and in transverse direction ($r = 0.078$, $n = 32$, $p = 0.673$). Equally, there is also no 255   significant correlation between shear modulus and depth in longitudinal direction $r = 0.115$, $n = 32$, $p = 0.531$) and in transverse direction ($r = 0.045$, $n = 32$, $p = 0.809$). For consolidated pack ice, there no significant correlation between Young's modulus and depth in longitudinal direction ($r = -0.413$, $n = 11$, $p = 0.207$), however, there is a significant negative correlation in transverse direction ($r = -0.672$, $n = 11$, $p = 0.024$). Similarly, there is no significant correlation between shear modulus and depth in longitudinal direction ($r = -0.425$, $n = 11$, $p = 0.192$), but there is a significant negative correlation 260   in transverse direction ($r = -0.665$, $n = 11$, $p = 0.026$). As the brine volume is increasing with depth for consolidated pack ice as shown in Fig. 8, this negative correlation is in-line what has been reported in literature, see e.g. Langleben and Pounder (1963); Mellor (1986); Moslet (2007).
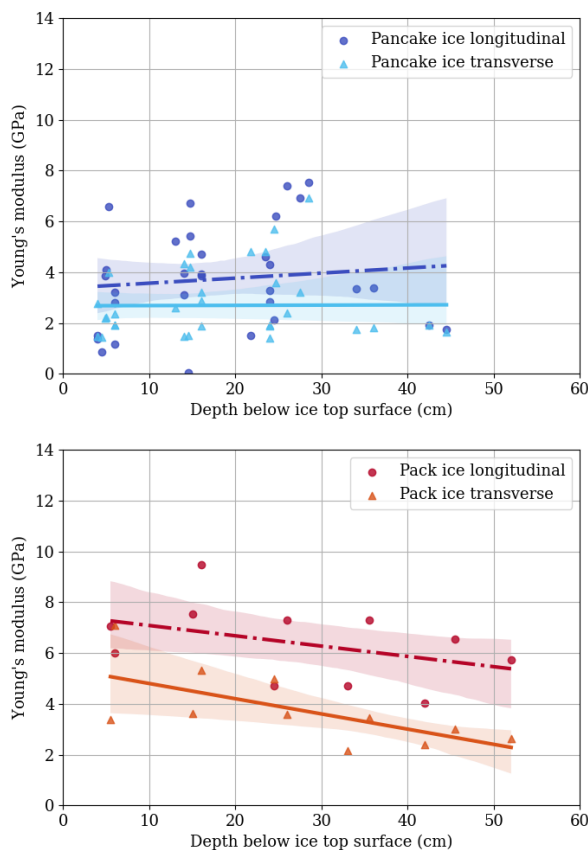
Figure 11. Longitudinal and transverse Young's modulus for pancake ice cores M01-US-01-A/B/C/D and M01-US-02-A/B/C/D as well as consolidated pack ice cores M03-US-01-A and M03-US-02-A as a function of depth from the top of the ice. The shading indicates the 90-percentile confidence intervals.

With substantially lower temperature and brine values as shown in Figs. 6 and 8, respectively, the elastic properties found for consolidated pack ice exhibit higher values than for pancake ice, in particular for the upper core sections, with values in

265 longitudinal direction of $6.4 \pm 1.6\,\mathrm{GPa}$ and $2.3 \pm 0.6\,\mathrm{GPa}$ for the Young's and the shear modulus, respectively, as opposed to $3.7 \pm 2.0\,\mathrm{GPa}$ and $1.3 \pm 0.7\,\mathrm{GPa}$, respectively. Also, the textural differences between both ice types can be expected to contribute to this discrepancy. The stratigraphical data found for consolidated pack ice (Fig. 10) indicates granular layers intermixed with transitional and columnar layers located in the upper half of the core whereas pancake ice is almost exclusively granular. The dynamic Young's and shear moduli for both ice types are generally lower than reported in literature for columnar

270 first-year ice at low brine volumes given as 9.0-$9.5\,\mathrm{GPa}$ (Mellor, 1986) and 3.0-$3.5\,\mathrm{GPa}$ (Snyder et al., 2015), respectively. For the consolidated pack ice, this is most likely due to the high granular ice content as temperature and salinity values are comparable.
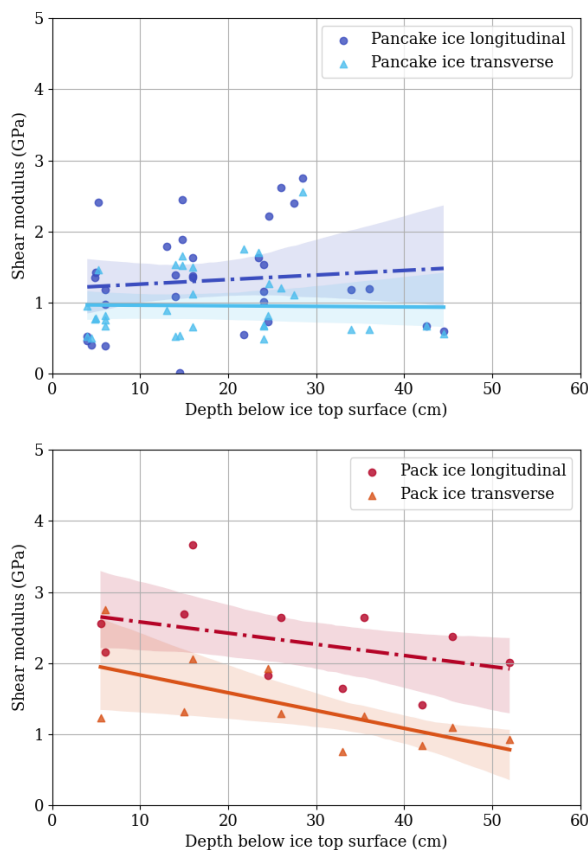
Figure 12. Longitudinal and transverse shear modulus for pancake ice cores M01-US-01-A/B/C/D and M01-US-02-A/B/C/D as well as consolidated pack ice cores M03-US-01-A and M03-US-02-A as a function of depth from the top of the ice. The shading indicates the 90-percentile confidence intervals.

In the sea ice studies by Sinha (1984) and Nanthikesan and Sunder (1994) based on the experiments by Dantl (1969) as well as Gammon et al. (1983), polycrystalline sea ice is found to exhibit only a very slight directional dependency in terms of
275   elastic material properties. In contrast, the results shown in Figs. 11 and 12 indicate a significant difference of elastic moduli measured in longitudinal and transverse core directions, respectively, in particular for the consolidated pack ice where the latter was determined as $3.8 \pm 1.5\,\mathrm{GPa}$ and $1.4 \pm 0.6\,\mathrm{GPa}$ for the Young's and the shear modulus, respectively. Based on the previous studies mentioned before, the finding of directional dependence of elastic properties in this magnitude is unprecedented, in particular considering the predominantly granular ice composition. The pore and channel structure might be of influence
280   which, for consolidated pack ice, can be expected to increase with depth leading to the formation of predominantly vertically aligned brine channels which potentially alter the directional dependency of elastic ice properties with depth.

Combining brine volume and Young's modulus datasets Figs. 8, 11 and 12, respectively, the dependency of the Young's modulus on the relative brine volume is obtained as shown in Fig. 13. There is a significant negative correlation between Young's
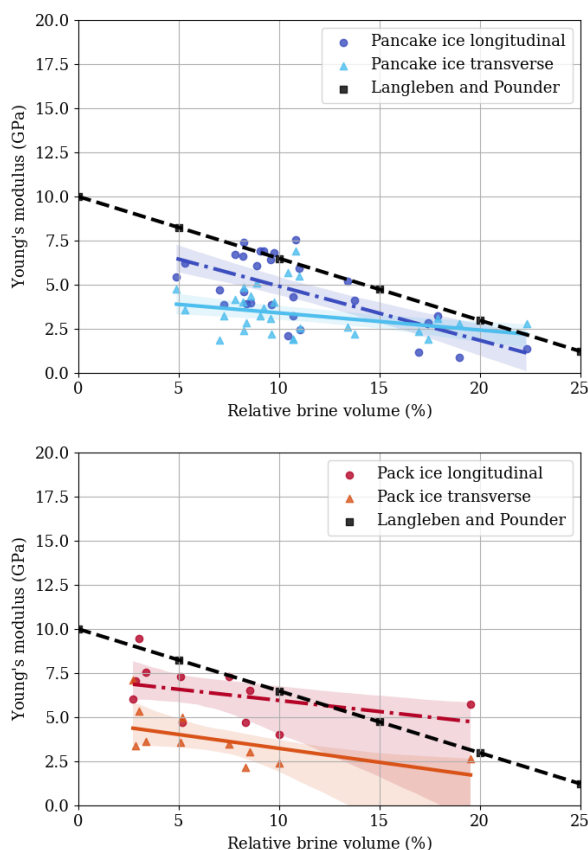
Figure 13. Longitudinal and transverse Young's modulus for pancake ice cores M01-US-01-A/B/C/D and M01-US-02-A/B/C/D as well as consolidated pack ice cores M03-US-01-A and M03-US-02-A as a function of percentage porosity of total volume. The shading indicates the 90-percentile confidence intervals.

modulus and brine volume for pancake ice in longitudinal direction ($r = -0.657$, $n = 29$, $p < 0.001$) and in transverse direc-
tion ($r = -0.308$, $n = 29$, $p = 0.104$). For consolidated pack ice, there is no significant correlation between Young's modulus and brine volume in longitudinal direction ($r = -0.428$, $n = 11$, $p = 0.189$) but there is a significant negative correlation in transverse direction ($r = -0.579$, $n = 11$, $p = 0.062$). A remarkable aspect of the obtained data is the noticeable directional dependency of the stiffness-porosity relation, as the Young's modulus, in particular in transverse direction, follows distinctly lower trend-lines in terms of magnitude than predicted by the relation found by Langleben and Pounder (1963) for Arctic ice indicated by the dashed black line in Fig. 13 which is expressed as

$$E(\text{GPa}) = 10.0 - 35.1\,V_b\,.$$

3.4 Compressive strength

Compressive strength of Antarctic sea ice in winter has only been studied by Urabe and Inoue (1988), but the testing was done after long storage-time at $-20\,°C$. In contrast, the compressive stress-time plots for the fifteen cores displayed in Fig. 14 have been obtained in situ within two hours of collection. The uniaxial compressive strength for pancake ice and consolidated pack ice were determined as $2.3 \pm 0.5\,MPa$ and $4.1 \pm 0.9\,MPa$, respectively. All tests shown in Fig. 14 are characterized by ductile failure behaviour with initial strain hardening and significant strain softening after the peak stress has been reached. For columnar ice, Kuehn and Schulson (1994) found the ductile-brittle failure transition at a strain rate of $2 \times 10^{-4}\,s^{-1}$. However, it was stated to be one order of magnitude higher for granular ice which can be confirmed by our results obtained for a strain rate of $5 \times 10^{-4}\,s^{-1}$.

The Antarctic sea ice compressive strength results by Urabe and Inoue (1988) of about $8.5\,MPa$ for vertical tested samples at a strain rate of around $1 \times 10^{-4}\,s^{-1}$ are higher than our strength measurements for consolidated pack ice. However, they tested land-fast sea ice. The compression strength data by Kivimaa and Kosloff (1994a) obtained in the Weddell Sea in situ in spring are in the range from $1.2\,MPa$ to $4.5\,MPa$ at a strain rate of $1 \times 10^{-3}\,s^{-1}$, which, despite the brittle failure regime, is lower than the consolidated pack ice data we obtained.

It is known from literature, that a decrease in ice temperature results in a higher compressive strength (Han et al., 2015; Kermani et al., 2007). This linkage can be confirmed for the tested consolidated pack ice considering the depth-evolution of both, the increasing temperature illustrated in Fig. 6 and the decreasing maximum stress ($r = -0.632$, $n = 8$, $p = 0.093$) depicted in Fig. 15. For the tested pancake ice, this relationship cannot be observed as the maximum uniaxial compressive stress monotonously increases with depth ($r = -0.452$, $n = 19$, $p = 0.052$) and temperature. The increase of pancake ice compressive strength over depth can be fitted by the following linear trend-line

$$\sigma_{\text{compression}} = (4.4 \cdot d + 1.6)\,MPa \tag{4}$$

where d denotes the depth in meter. This discrepancy between the tested consolidated pack and pancake ice can be explained by the high salinity values and brine volumes at the top of the pancake ice floes which show the opposite trend compared with the consolidated pack ice as illustrated in Fig. 8. Kovacs (1997) proposed a relation based on total porosity and strain rate to estimate the compressive strength of Arctic first-year sea ice. Fig. 16 compares this relation with the measured compressive strength of pancake ice and consolidated pack ice making use of the porosity data given in Fig. 8 and assuming negligible air volume fraction (Ehn et al., 2007). Despite textural differences, the Antarctic compression strength data show the same trend as the equation derived by Kovacs (1997) for Arctic ice.

Sinha (1984) reported an increasing ice strength with depth in horizontally tested hummock ice of an old floe. Kivimaa and Kosloff (1994b) as well as Urabe and Inoue (1988) found that the maximum compressive strength was reached in a middle layer of the ice sheet. In the study by Frederking and Timco (1983), a difference was also observed between top and bottom layers where the latter exhibits a larger strength magnitude. This is in contrast to our findings regarding consolidated pack ice which is strongest at the top and exhibits decreasing strength towards the middle layer due to the increasing brine volume with depth.
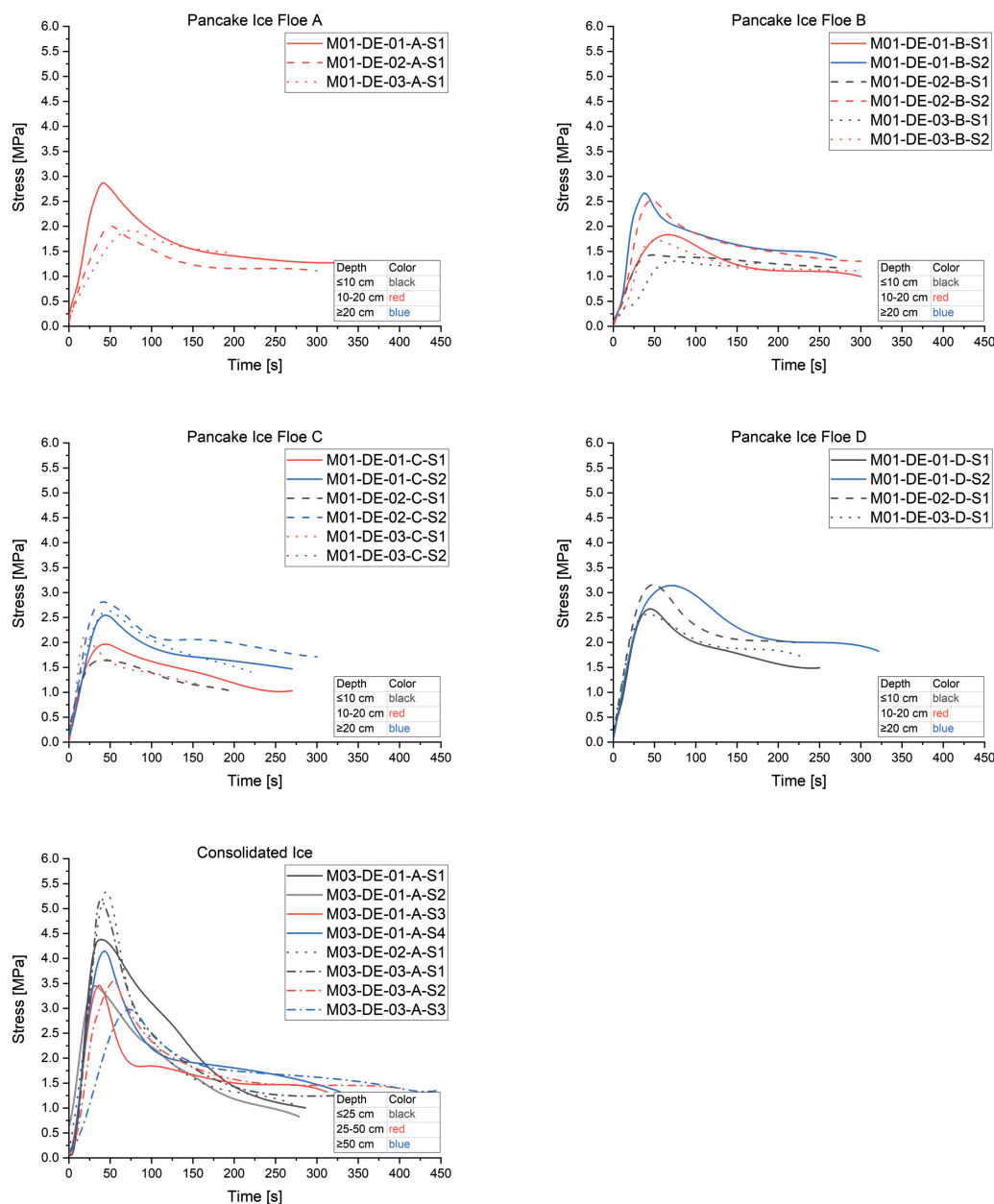
Figure 14. Stress-time plots of uniaxial compression test results for all specimens, respective pancake ice floes and consolidated pack ice. The color-coding refers to the sample depth in cm along the core length measured at the sample center and the line style to the specific core.

Both, consolidated pack and pancake ice investigated in this study, are relatively young first-year ice which has been collected in the Antarctic MIZ during the winter season when sea ice was advancing and was exposed to high temperature gradients. In this sense, its measured strength properties are therefore not directly comparable to those mentioned before.
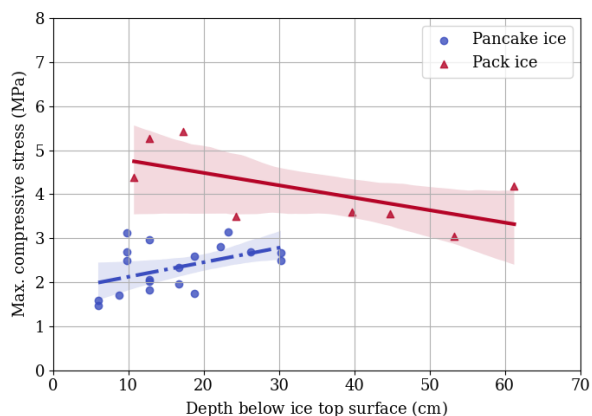
Figure 15. Maximum uniaxial compressive stress for pancake and pack ice over depth with the 90-percentile confidence intervals indicated.
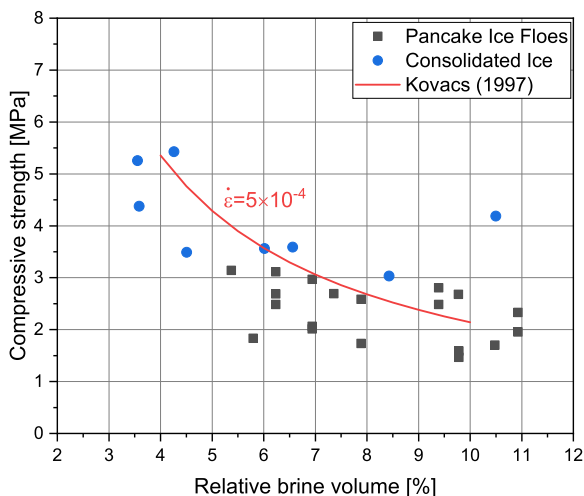
Figure 16. Uniaxial compressive strength for pancake ice and consolidated ice against brine volume as compared to the relation found by Kovacs (1997) using the strain rate of $5 \times 10^{-4}\,\mathrm{s}^{-1}$ applied to obtain the here reported data.

4 Conclusions

330 The collected data sets of young first-year ice combined physical, morphological and mechanical in situ test results of solitary pancake ice floes and consolidated pack ice representing a vertical $150\,\mathrm{km}$-transect into the advancing Antarctic marginal ice zone along the Good Hope Line. Of particular interest was to elucidate the transition between both ice types within the MIZ

in terms of their differences in mechanical stiffness and strength properties as linked to physical and textural characteristics at early-stage ice formation.

335   Both ice types exhibited a characteristic linear temperature profile with depth and had predominantly granular textures, for pancake ice almost exclusively, due to the highly dynamic ocean environment. Pancake ice floe C, however, had an almost constant and fairly high temperature distribution which was attributed to overwashing during collection and subsequent vertical drainage. The pancake ice salinity profile exhibited very high magnitudes at the topmost sections and and in the snow cover. Accordingly, overwashing and flooding events are a reasonable explanation for the generally high pancake ice salinity at the

340   topmost sections, in particular, as the consolidated pack ice had a very low salinity value at the top, slightly increasing toward the bottom, where recent flooding events can be excluded.

The dynamic Young's and shear moduli measured for consolidated pack ice were substantially lower than reported in literature for first-year ice. The elastic properties of pancake ice were even lower in magnitude due to the high brine volume content and higher temperatures. A similar trend could be observed for the uniaxial compression strength which was found

345   to be lower than reported by the only available source in literature for winter Antarctic sea ice, albeit land-fast, by Urabe and Inoue (1988). For pancake ice, the uniaxial compression strength linearly increased with depth as opposed to the consolidated pack ice which decreased with depth as typically reported in literature (Han et al., 2015; Kermani et al., 2007). A distinct directional dependency of the elastic moduli in vertical and horizontal directions, respectively, has been found, in particular for consolidated pack ice. Interestingly, the elastic anisotropy of sea ice has not found much attention in literature and has been

350   considered of minor significance. Clearly, besides temperature, ice morphology and age have an at least equal influence on sea ice stiffness and strength. In particular, the remarkable vertical strength and stiffness profiles of pancake ice floes cannot be exclusively explained by temperature data but need to include salinity, brine volume and textural information as well.

In summary, there is a complete lack of data concerning the mechanical behaviour of winter first-year sea ice in the Antarctic. The physical and mechanical sea ice properties obtained for young mostly granular Antarctic first-year ice exhibited distinct

355   differences to measurements done on Arctic predominantly columnar sea ice in terms of compression strength, stiffness and directional dependency of elastic moduli warranting further studies to elucidate the influence of environmental conditions characteristic for the Antarctic marginal ice zone on the interrelation of morphological and physical with the mechanical sea ice properties.

Data availability. All experimental data part of this manuscript have been made available via a publically accessible data repository https:

360   //doi.org/10.25375/uct.14900361.

Appendix A: Pancake and consolidated pack ice core lists

A1 Consolidated pack ice data

Table A1. Overview of pack ice core IDs, corresponding core names, testing designation, and date and time when cored.

Core ID	Core Name	Test Designation	Date Cored	Time Cored
1	M03-TM-01-A	Trace metal	July 27, 2019	10am-4pm (UTC)
2	M03-TM-02-A	Trace metal	July 27, 2019	10am-4pm (UTC)
3	M03-TM-03-A	Trace metal	July 27, 2019	10am-4pm (UTC)
4	M03-TM-04-A	Trace metal	July 27, 2019	10am-4pm (UTC)
5	M03-TM-05-A	Trace metal	July 27, 2019	10am-4pm (UTC)
6	M03-BGC-01-A	Isotope	July 27, 2019	10am-4pm (UTC)
7	M03-BGC-02-A	Isotope	July 27, 2019	10am-4pm (UTC)
8	M03-PHY-01-A	Temperature	July 27, 2019	10am-4pm (UTC)
9	M03-PHY-02-A	Temperature	July 27, 2019	10am-4pm (UTC)
10	M03-PHY-03-A	Temperature	July 27, 2019	10am-4pm (UTC)
11	M03-CPUT-01-A	Biology	July 27, 2019	10am-4pm (UTC)
12	M03-CPUT-02-A	Biology	July 27, 2019	10am-4pm (UTC)
13	M03-BIO-01-A	Bio-cultivation	July 27, 2019	10am-4pm (UTC)
14	M03-CT-01-A	MicroCT	July 27, 2019	10am-4pm (UTC)
15	M03-CT-02-A	MicroCT	July 27, 2019	10am-4pm (UTC)
16	M03-CP-01-A	Morphology	July 27, 2019	10am-4pm (UTC)
17	M03-CP-02-A	Morphology	July 27, 2019	10am-4pm (UTC)
18	M03-US-01-A	Elasticity	July 27, 2019	10am-4pm (UTC)
19	M03-US-02-A	Elasticity	July 27, 2019	10am-4pm (UTC)
20	M03-US-03-A	Elasticity	July 27, 2019	10am-4pm (UTC)
21	M03-DE-01-A	Compression strength	July 27, 2019	10am-4pm (UTC)
22	M03-DE-02-A	Compression strength	July 27, 2019	10am-4pm (UTC)
23	M03-DE-03-A	Compression strength	July 27, 2019	10am-4pm (UTC)

A1 Pancake ice cores
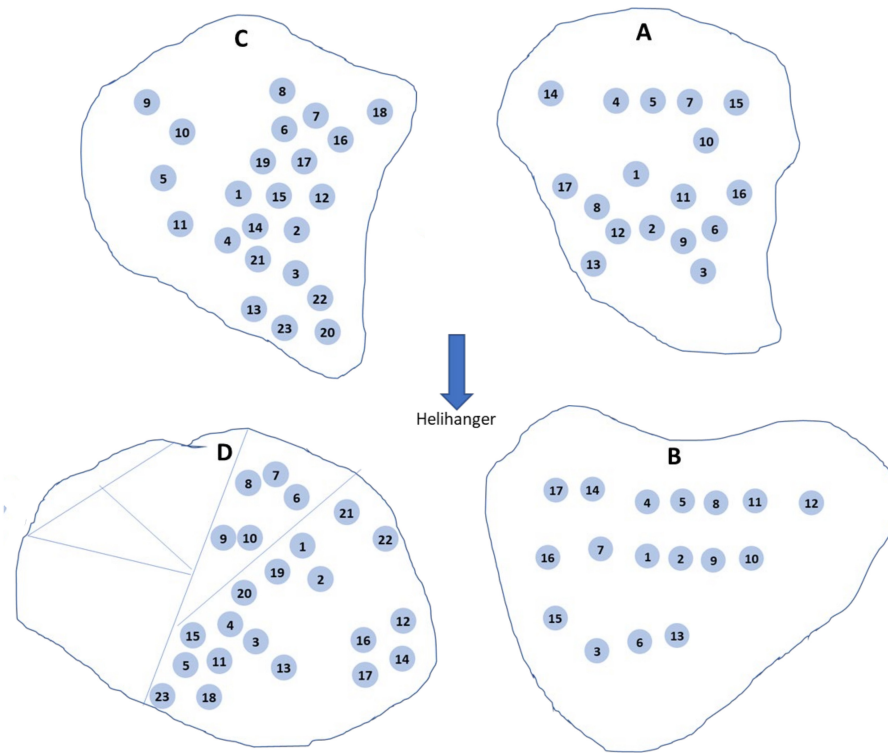
Figure A1. Coring layout for pancake ice floes A, B, C and D, respectively.

Table A2. Overview of core IDs of pancake A, corresponding core names, testing designation, and date and time when cored.

Core ID	Core Name	Test Designation	Date Cored	Time Cored
1	M01-PHY-01-A	Temperature	July 28, 2019	10:50am (UTC)
2	M01-BGC-01-A	Isotope	July 28, 2019	11:05am (UTC)
3	M01-PHY-02-A	Temperature	July 28, 2019	11:10am (UTC)
4	M01-BGC-02-A	Isotope	July 28, 2019	11:12am (UTC)
5	M01-PHY-03-A	Temperature	July 28, 2019	11:15am (UTC)
6	M01-CPUT-01-A	Biology	July 28, 2019	11:30am (UTC)
7	M01-CPUT-02-A	Biology	July 28, 2019	11:32am (UTC)
8	M01-CT-01-A	MicroCT	July 28, 2019	11:50am (UTC)
9	M01-CT-02-A	MicroCT	July 28, 2019	11:52am (UTC)
10	M01-CP-01-A	Morphology	July 28, 2019	12:01pm (UTC)
11	M01-CP-02-A	Morphology	July 28, 2019	12:05pm (UTC)
12	M01-US-01-A	Elasticity	July 28, 2019	12:06pm (UTC)
13	M01-US-02-A	Elasticity	July 28, 2019	12:11pm (UTC)
14	M01-US-03-A	Elasticity	July 28, 2019	12:13pm (UTC)
15	M01-DE-01-A	Compression strength	July 28, 2019	12:18pm (UTC)
16	M01-DE-02-A	Compression strength	July 28, 2019	12:19pm (UTC)
17	M01-DE-03-A	Compression strength	July 28, 2019	12:22pm (UTC)

Table A3. Overview of core IDs of pancake B, corresponding core names, testing designation, and date and time when cored.

Core ID	Core Name	Core Type	Date Cored	Time Cored
1	M01-PHY-01-B	Temperature	July 28, 2019	11:05am (UTC)
2	M01-BGC-01-A	Isotope	July 28, 2019	11:18am (UTC)
3	M01-PHY-02-B	Temperature	July 28, 2019	11:20am (UTC)
4	M01-BGC-02-B	Isotope	July 28, 2019	11:24am (UTC)
5	M01-PHY-03-B	Temperature	July 28, 2019	11:26am (UTC)
6	M01-CPUT-01-B	Biology	July 28, 2019	11:35am (UTC)
7	M01-CPUT-02-B	Biology	July 28, 2019	11:40am (UTC)
8	M01-CT-01-B	MicroCT	July 28, 2019	11:57am (UTC)
9	M01-CT-02-B	MicroCT	July 28, 2019	11:59am (UTC)
10	M01-CP-01-B	Morphology	July 28, 2019	12:35pm (UTC)
11	M01-CP-02-B	Morphology	July 28, 2019	12:47pm (UTC)
12	M01-US-01-B	Elasticity	July 28, 2019	12:50pm (UTC)
13	M01-US-02-B	Elasticity	July 28, 2019	12:52pm (UTC)
14	M01-US-03-B	Elasticity	July 28, 2019	1:38pm (UTC)
15	M01-DE-01-B	Compression strength	July 28, 2019	2:06pm (UTC)
16	M01-DE-02-B	Compression strength	July 28, 2019	2:09pm (UTC)
17	M01-DE-03-B	Compression strength	July 28, 2019	2:11pm (UTC)

Table A4. Overview of core IDs of pancake C, corresponding core names, testing designation, and date and time when cored.

Core ID	Core Name	Core Type	Date Cored	Time Cored
1	M01-PHY-01-C	Temperature	July 28, 2019	1:05pm (UTC)
2	M01-BGC-01-C	Isotope	July 28, 2019	1:06pm (UTC)
3	M01-PHY-02-C	Temperature	July 28, 2019	1:18pm (UTC)
4	M01-BGC-02-C	Isotope	July 28, 2019	1:22pm (UTC)
5	M01-PHY-03-C	Temperature	July 28, 2019	1:26pm (UTC)
6	M01-TM-01-C	Trace metal	July 28, 2019	1:47pm (UTC)
7	M01-TM-02-C	Trace metal	July 28, 2019	1:53pm (UTC)
8	M01-TM-03-C	Trace metal	July 28, 2019	1:56pm (UTC)
9	M01-TM-04-C	Trace metal	July 28, 2019	2:14pm (UTC)
10	M01-TM-05-C	Trace metal	July 28, 2019	2:18pm (UTC)
11	M01-CP-01-C	Trace metal	July 28, 2019	2:23pm (UTC)
12	M01-CPUT-01-C	Biology	July 28, 2019	3:40pm (UTC)
13	M01-CPUT-02-C	Biology	July 28, 2019	3:42pm (UTC)
14	M01-CT-01-C	MicroCT	July 28, 2019	3:44pm (UTC)
15	M01-CT-02-C	MicroCT	July 28, 2019	3:45pm (UTC)
16	M01-CP-02-C	Morphology	July 28, 2019	3:47pm (UTC)
17	M01-US-01-C	Elasticity	July 28, 2019	3:50pm (UTC)
18	M01-US-02-C	Elasticity	July 28, 2019	3:51pm (UTC)
19	M01-US-03-C	Elasticity	July 28, 2019	3:53pm (UTC)
20	M01-DE-01-C	Compression strength	July 28, 2019	3:57pm (UTC)
21	M01-DE-02-C	Compression strength	July 28, 2019	3:58pm (UTC)
22	M01-DE-03-C	Compression strength	July 28, 2019	4pm (UTC)

Table A5. Overview of core IDs of pancake D, corresponding core names, testing designation, and date and time when cored.

Core ID	Core Name	Core Type	Date Cored	Time Cored
1	M01-PHY-01-D	Temperature	July 28, 2019	1:13pm (UTC)
2	M01-BGC-01-D	Isotope	July 28, 2019	1:16pm (UTC)
3	M02-BGC-01-D	Isotope	July 28, 2019	1:30pm (UTC)
4	M01-PHY-02-D	Temperature	July 28, 2019	1:35pm (UTC)
5	M01-PHY-03-D	Temperature	July 28, 2019	1:40pm (UTC)
6	M01-TM-01-D	Trace metal	July 28, 2019	2:34pm (UTC)
7	M01-TM-02-D	Trace metal	July 28, 2019	2:36pm (UTC)
8	M01-TM-03-D	Trace metal	July 28, 2019	2:39pm (UTC)
9	M01-TM-04-D	Trace metal	July 28, 2019	2:42pm (UTC)
10	M01-TM-05-D	Trace metal	July 28, 2019	2:44pm (UTC)
11	M01-CPUT-01-D	Biology	July 28, 2019	2:52pm (UTC)
12	M01-CPUT-02-D	Biology	July 28, 2019	2:55pm (UTC)
13	M01-CT-01-D	MicroCT	July 28, 2019	2:59pm (UTC)
14	M01-CT-02-D	MicroCT	July 28, 2019	3:02pm (UTC)
15	M01-US-01-D	Elasticity	July 28, 2019	3:07pm (UTC)
16	M01-US-02-D	Elasticity	July 28, 2019	3:11pm (UTC)
17	M01-US-03-D	Elasticity	July 28, 2019	3:14pm (UTC)
18	M01-CP-01-D	Morphology	July 28, 2019	3:19pm (UTC)
19	M01-CP-02-D	Morphology	July 28, 2019	3:20pm (UTC)
20	M01-DE-01-D	Compression strength	July 28, 2019	3:22pm (UTC)
21	M01-DE-02-D	Compression strength	July 28, 2019	3:26pm (UTC)
22	M01-DE-03-D	Compression strength	July 28, 2019	3:30pm (UTC)
23	M01-CPUT-03-D	Biology	July 28, 2019	3:35pm (UTC)

Appendix B: Core segmentation for elasticity and uniaxial compression strength testing
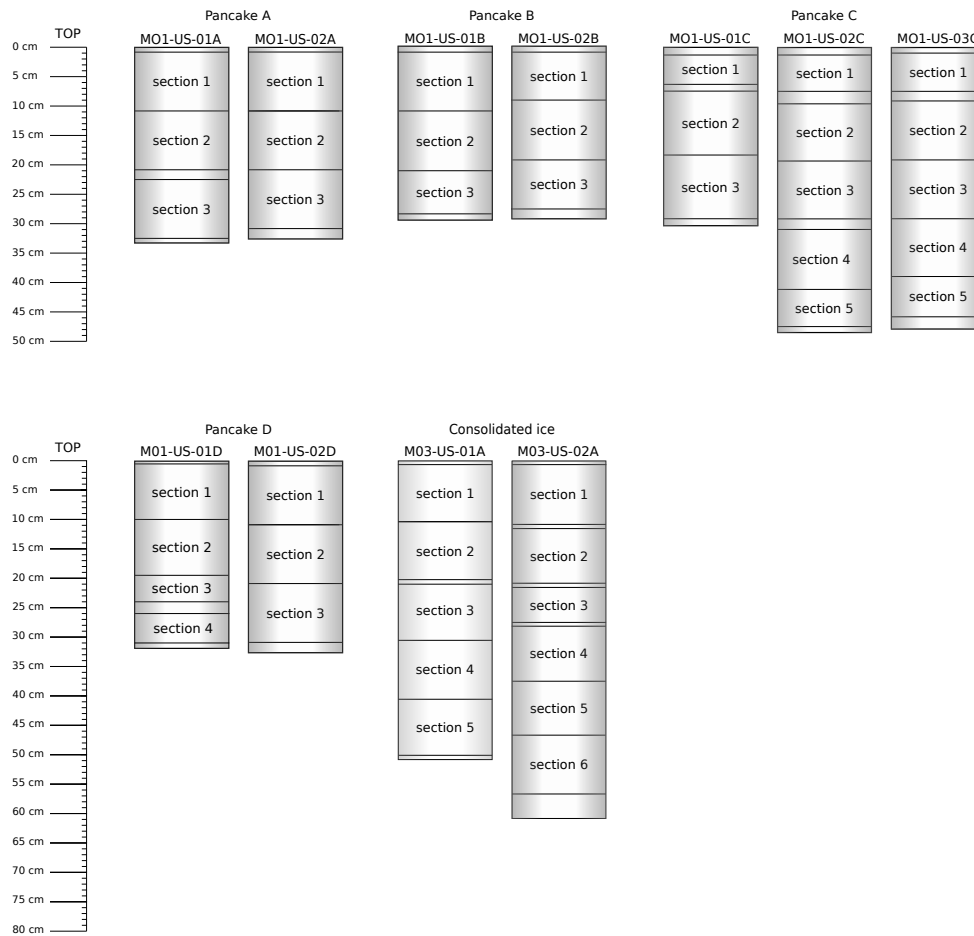
Figure B1. Schematic of the segmentation of seven pancake ice and two pack ice cores subjected to ultrasound testing with section dimensions and corresponding section numbering.
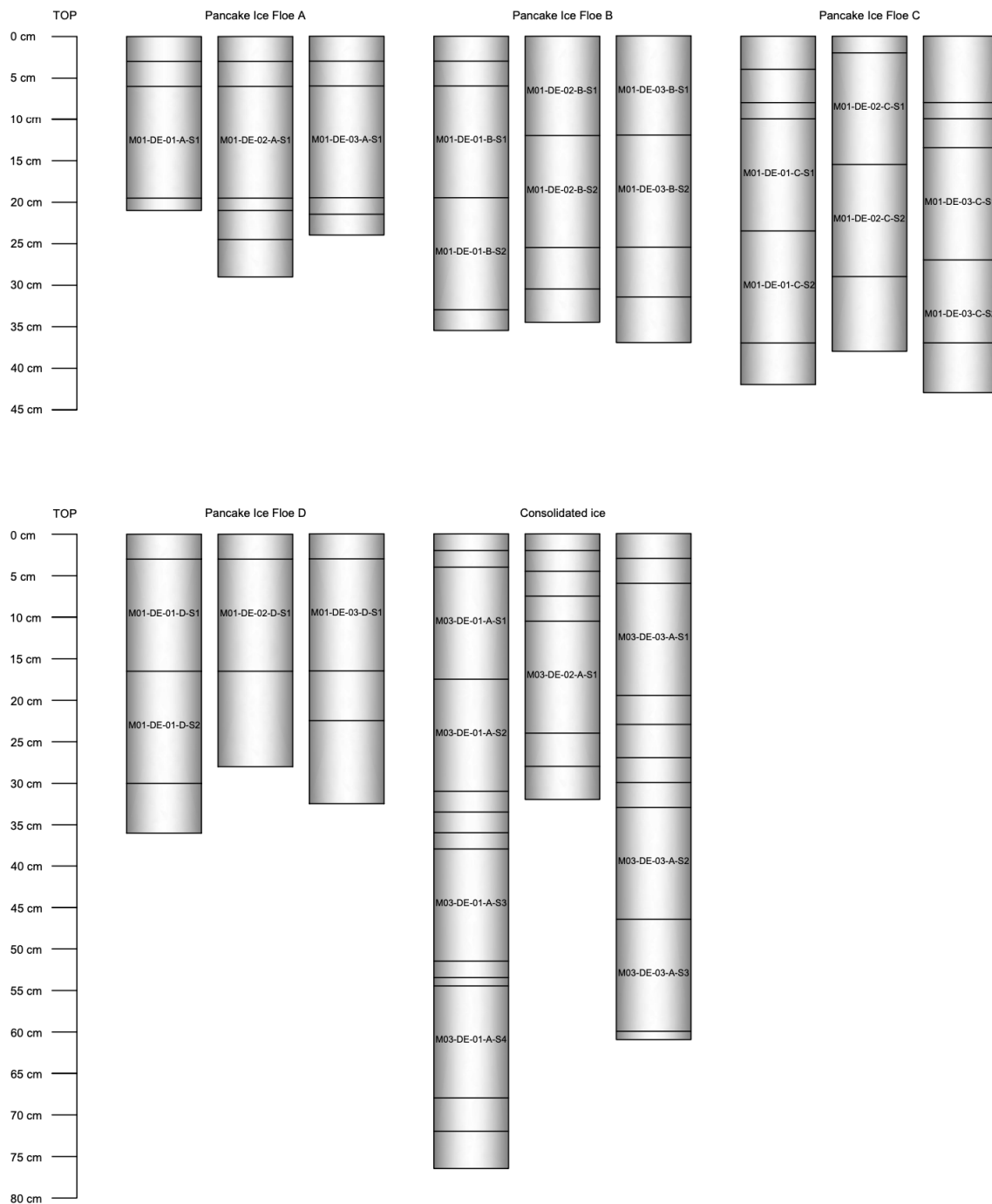
Figure B2. Schematic of the segmentation of twelve pancake ice and three pack ice cores subjected to compression testing with sample dimensions and corresponding core names.

365 *Author contributions.* Conceptualization by SS, DL, KM, TM, and MV. Morphological analysis methodology developed by SJ and TR, ultrasound testing methodology developed by SS, KM and RM, uniaxial compression testing methodology developed by DL, TM and FP. Investigation and data curation by SS, RA, AC, EH, SJ, KM RM, TM, EM, FP, TR and CS. Formal analysis by SS, RA, AC, SJ, DL, KM, RM, TM and FP. Funding acquisition by SS, DL, JS and MV. The original draft was written by SS with assistance from all co-authors.

Competing interests. The authors declare that the research was conducted in the absence of any commercial or financial relationships that

370 could be construed as a potential conflict of interest.

Acknowledgements. This research has been funded by the National Research Foundation of South Africa (NRF) (Grant Nos. 104839, 105858 and 118745). Opinions expressed and conclusions arrived at are those of the author and are not necessarily to be attributed to the NRF. SS, RA, AC, EH, RM, EM, TR and MV acknowledge support from the South African National Antarctic Programme (SANAP).

References

375   Bennetts, L., O'Farrell, S., and Uotila, P.: Brief communication: Impacts of ocean-wave-induced breakup of Antarctic sea ice via thermodynamics in a stand-alone version of the CICE sea-ice model, The Cryosphere, 2017.

Bromwich, D. H., Guo, Z., Bai, L., and Chen, Q.-s.: Modeled Antarctic precipitation. Part I: Spatial and temporal variability, Journal of Climate, 17, 427–447, 2004.

Carnat, G., Papakyriakou, T., Geilfus, N.-X., Brabant, F., Delille, B., Vancoppenolle, M., Gilson, G., Zhou, J., and Tison, J.-L.: Investigations

380   on physical and textural properties of Arctic first-year sea ice in the Amundsen Gulf, Canada, November 2007–June 2008 (IPY-CFL system study), Journal of Glaciology, 59, 819–837, 2013.

Dantl, G.: Elastic moduli of ice, in: Physics of ice: proceedings of the International Symposium on Physics of Ice, Munich, Germany, September 9–14, 1968, edited by Camp, P., Kiszenick, W., Arnold, D., Riehl, N., Bullemer, B., Engelhardt, H., et al., pp. 223–230, 1969.

de Vos, M., Barnes, M., Biddle, L. C., Swart, S., Ramjukadh, C.-L., and Vichi, M.: Evaluating numerical and free-drift forecasts of sea ice

385   drift during a Southern Ocean research expedition: An operational perspective, Journal of Operational Oceanography, pp. 1–17, 2021.

Dempsey, D. and Langhorne, P.: Geometric properties of platelet ice crystals, Cold regions science and technology, 78, 1–13, 2012.

Ehn, J. K., Hwang, B. J., Galley, R., and Barber, D. G.: Investigations of newly formed sea ice in the Cape Bathurst polynya: 1. Structural, physical, and optical properties, Journal of Geophysical Research: Oceans, 112, 1–15, https://doi.org/10.1029/2006JC003702, 2007.

Eicken, H.: Deriving modes and rates of ice growth in the Weddell Sea from microstructural, salinity and stable-isotope data, Antarctic Sea

390   Ice: Physical Processes, Interactions and Variability, Antarct. Res. Ser, 74, 89–122, 1998.

Eicken, H., Lange, M. A., and Wadhams, P.: Characteristics and distribution patterns of snow and meteoric ice in the Weddell Sea and their contribution to the mass balance of sea ice, in: Annales Geophysicae, vol. 12, pp. 80–93, Springer, 1994.

Eicken, H., Fischer, H., and Lemke, P.: Effects of the snow cover on Antarctic sea ice and potential modulation of its response to climate change, Annals of Glaciology, 21, 369–376, 1995.

395   Frankenstein, G. and Garner, R.: Equations for determining the brine volume of sea ice from -0.5^o to -22.9^o C, Journal of Glaciology, 6, 943–944, 1967.

Frederking, R. and Timco, G.: Uniaxial compressive strength and deformation of Beaufort sea ice, in: The Seventh International Conference on Port and Ocean Engineering under Arctic Conditions, pp. 89–98, 1983.

Galley, R., Else, B., Geilfus, N.-X., Hare, A., Isleifson, D., Barber, D., and Rysgaard, S.: Imaged brine inclusions in young sea ice—Shape,

400   distribution and formation timing, Cold Regions Science and Technology, 111, 39–48, 2015.

Gammon, P., Kiefte, H., Clouter, M., and Denner, W.: Elastic constants of artificial and natural ice samples by Brillouin spectroscopy, Journal of glaciology, 29, 433–460, 1983.

Haas, C., Vieho, T., and Eicken, H.: Sea-ice conditions during the Winter Weddell Gyre Study 1992, ANT X/4, with RV" Polarstern": Ship observations and AVHRR satellite imagery, Berichte aus dem Fachbereich Physik, 34, 1992.

405   Han, H., Li, Z., Huang, W., Lu, P., and Lei, R.: The uniaxial compressive strength of the Arctic summer sea ice, Acta Oceanologica Sinica, 34, 129–136, https://doi.org/10.1007/s13131-015-0598-7, 2015.

Hepworth, E., Vichi, M., van Zuydam, A., Taylor, N. C., Bossau, J., Engelbrecht, M., and Aarskog, T.: Sea Ice Observations in the Antarctic Marginal Ice Zone during Winter 2019, https://doi.org/10.1594/PANGAEA.921759, 2020.

Hibler III, W.: A dynamic thermodynamic sea ice model, Journal of physical oceanography, 9, 815–846, 1979.

410   Hobbs, W. R., Massom, R., Stammerjohn, S., Reid, P., Williams, G., and Meier, W.: A review of recent changes in Southern Ocean sea ice, their drivers and forcings, Global and Planetary Change, 143, 228–250, 2016.

Hutchings, J. and Hibler III, W.: Small-scale sea ice deformation in the Beaufort Sea seasonal ice zone, Journal of Geophysical Research: Oceans, 113, 2008.

Hutchings, J., Heil, P., Steer, A., and Hibler III, W.: Subsynoptic scale spatial variability of sea ice deformation in the western Weddell Sea

415   during early summer, Journal of Geophysical Research: Oceans, 117, 2012.

Jeffries, M. O., Shaw, R. A., Morris, K., Veazey, A. L., and Krouse, H. R.: Crystal structure, stable isotopes (δ18O), and development of sea ice in the Ross, Amundsen, and Bellingshausen seas, Antarctica, Journal of Geophysical Research: Oceans, 99, 985–995, 1994.

Jeffries, M. O., Krouse, H. R., Hurst-Cushing, B., and Maksym, T.: Snow-ice accretion and snow-cover depletion on Antarctic first-year sea-ice floes, Annals of Glaciology, 33, 51–60, 2001.

420   Kermani, M., Farzaneh, M., and Gagnon, R.: Compressive strength of atmospheric ice, Cold Regions Science and Technology, 49, 195–205, https://doi.org/10.1016/j.coldregions.2007.05.003, 2007.

Kivimaa, S. and Kosloff, P.: Compressive Strength And Structure Of Sea Ice In The Weddell Sea, Antarctica, The Built Environment, 5, 12, 1994a.

Kivimaa, S. and Kosloff, P.: Compressive strength and structure of sea ice in the Weddell Sea, Antarctica, WIT Transactions on The Built

425   Environment, 5, 1994b.

Kovacs, A.: Sea ice. Part II, Estimating the full-scale tensile, flexural and compressive strength of first-year ice, 1996.

Kovacs, A.: Estimating the full-scale flexural and compressive strength of first-year sea ice, Journal of Geophysical Research: Oceans, 102, 8681–8689, https://doi.org/10.1029/96JC02738, 1997.

Kuehn, G. A. and Schulson, E. M.: The mechanical properties of saline ice under uniaxial compression, Annals of Glaciology, 19, 39–48,

430   1994.

Lange, M. and Eicken, H.: Textural characteristics of sea ice and the major mechanisms of ice growth in the Weddell Sea, Annals of Glaciology, 15, 210–215, 1991.

Lange, M., Schlosser, P., Ackley, S., Wadhams, P., and Dieckmann, G.: 18 O concentrations in sea ice of the Weddell Sea, Antarctica, Journal of Glaciology, 36, 315–323, 1990.

435   Lange, M. A., Ackley, S. F., Wadhams, P., Dieckmann, G., and Eicken, H.: Development of sea ice in the Weddell Sea, Annals of Glaciology, 12, 92–96, 1989.

Langleben, M. and Pounder, E.: Arctic Sea Ice of Various Ages, 1963.

Marquart, R., Bogaers, A., Skatulla, S., Alberello, A., Toffoli, A., Schwarz, C., and Vichi, M.: A computational fluid dynamics model for the small-scale dynamics of wave, ice floe and interstitial grease ice interaction, Fluids, 6, 176, 2021.

440   Massom, R., Lytle, V., Worby, A., and Allison, I.: Winter snow cover variability on East Antarctic sea ice, Journal of Geophysical Research: Oceans, 103, 24 837–24 855, 1998.

Mellor, M.: Mechanical behavior of sea ice, in: The geophysics of sea ice, pp. 165–281, Springer, 1986.

Melsheimer, C. and Spreen, G.: IUP Multiyear Ice Concentration and Other Sea Ice Types, Tech. Rep. Version 1.1 (Arctic)/Version AQ2 (Antarctic), Institute of Environmental Physics, University of Bremen, Bremen, 2021.

445   Moslet, P.: Field testing of uniaxial compression strength of columnar sea ice, Cold Regions Science and Technology, 48, 1–14, 2007.

Nakawo, M. and Sinha, N. K.: Growth rate and salinity profile of first-year sea ice in the high Arctic, Journal of Glaciology, 27, 315–330, 1981.

Nanthikesan, S. and Sunder, S. S.: Anisotropic elasticity of polycrystalline ice Ih, Cold regions science and technology, 22, 149–169, 1994.

Notz, D. and Worster, M. G.: In situ measurements of the evolution of young sea ice, Journal of Geophysical Research: Oceans, 113, 2008.

450 Paul, F., Mielke, T., Nisters, C., Schröder, J., Rampai, T., Skatulla, S., Audh, R., Hepworth, E., Vichi, M., and Lupascu, D. C.: Brief communication: Grease Ice in the Antarctic Marginal Ice Zone, Journal of Marine Science and Engineering, 2021.

Petrich, C. and Eicken, H.: Overview of sea ice growth and properties, in: Sea ice, edited by Thomas, D. N., pp. 1–41, John Wiley & Sons, Ltd Chichester, UK, 2017.

Provost, C., Sennéchael, N., Miguet, J., Itkin, P., Rösel, A., Koenig, Z., Villacieros-Robineau, N., and Granskog, M. A.: Observations of
455 flooding and snow-ice formation in a thinner Arctic sea-ice regime during the N-ICE2015 campaign: Influence of basal ice melt and storms, Journal of Geophysical Research: Oceans, 122, 7115–7134, 2017.

Pustogvar, A. and Kulyakhtin, A.: Sea ice density measurements. Methods and uncertainties, Cold Regions Science and Technology, 131, 46–52, https://doi.org/10.1016/j.coldregions.2016.09.001, 2016.

Roach, L. A., Horvat, C., Dean, S. M., and Bitz, C. M.: An emergent sea ice floe size distribution in a global coupled ocean-sea ice model,
460 Journal of Geophysical Research: Oceans, 123, 4322–4337, 2018.

Schulson, E., Fortt, A., Iliescu, D., and Renshaw, C.: Failure envelope of first-year Arctic sea ice: The role of friction in compressive fracture, Journal of Geophysical Research: Oceans, 111, 2006.

Schulson, E. M. and Duval, P.: Creep and Fracture of Ice, Cambridge University Press, Cambridge, https://doi.org/10.1017/CBO9780511581397, 2009.

465 Shokr, M. and Agnew, T. A.: Validation and potential applications of Environment Canada Ice Concentration Extractor (ECICE) algorithm to Arctic ice by combining AMSR-E and QuikSCAT observations, Remote sensing of environment, 128, 315–332, 2013.

Shokr, M. and Sinha, N.: Sea ice: physics and remote sensing, John Wiley & Sons, 2015.

Sinha, N. K.: Uniaxial compressive strength of first-year and multi-year sea ice, Canadian Journal of Civil Engineering, 11, 82–91, https://doi.org/10.1139/l84-010, 1984.

470 Smedsrud, L. H. and Skogseth, R.: Field measurements of Arctic grease ice properties and processes, Cold regions science and technology, 44, 171–183, 2006.

Snyder, S. A., Schulson, E. M., and Renshaw, C. E.: The role of damage and recrystallization in the elastic properties of columnar ice, Journal of Glaciology, 61, 461–480, https://doi.org/10.3189/2015JoG14J225, 2015.

Squire, V. A.: A fresh look at how ocean waves and sea ice interact, Philosophical Transactions of the Royal Society A: Mathematical,
475 Physical and Engineering Sciences, 376, 20170 342, 2018.

Sturm, M., Morris, K., and Massom, R.: The winter snow cover of the West Antarctic pack ice: its spatial and temporal variability, Antarctic sea ice: physical processes, interactions and variability, 74, 1–18, 1998.

Thomas, M., Vancoppenolle, M., France, J., Sturges, W., Bakker, D. C., Kaiser, J., and von Glasow, R.: Tracer measurements in growing sea ice support convective gravity drainage parameterizations, Journal of Geophysical Research: Oceans, 125, e2019JC015 791, 2020.

480 Timco, G. and Weeks, W.: A review of the engineering properties of sea ice, Cold regions science and technology, 60, 107–129, 2010.

Urabe, N. and Inoue, M.: Mechanical Properties of Antarctic Sea Ice, Journal of Offshore Mechanics and Arctic Engineering, 110, 403–408, https://doi.org/10.1115/1.3257079, 1988.

Wang, R. and Shen, H. H.: Gravity waves propagating into an ice-covered ocean: A viscoelastic model, Journal of Geophysical Research: Oceans, 115, 2010.

485 Weeks, W. F. and Ackley, S. F.: The growth, structure, and properties of sea ice, in: CRREL Monograph 82-1, pp. 1–130, CRREL, 1982.

Weiss, J. and Dansereau, V.: Linking scales in sea ice mechanics, Philosophical Transactions of the Royal Society A: Mathematical, Physical and Engineering Sciences, 375, 20150 352, 2017.

Wells, A., Wettlaufer, J., and Orszag, S.: Brine fluxes from growing sea ice, Geophysical Research Letters, 38, 2011.

Worby, A., Massom, R., Allison, I., Lytle, V., and Heil, P.: East Antarctic sea ice: A review of its structure, properties and drift, Antarctic sea
490   ice: physical processes, interactions and variability, 74, 41–67, 1998.

Ye, Y., Heygster, G., and Shokr, M.: Improving multiyear ice concentration estimates with reanalysis air temperatures, IEEE Transactions on Geoscience and Remote Sensing, 54, 2602–2614, 2015.